Southern Hemisphere Atmospheric Circulation Response to Global Warming

PAUL J. KUSHNER, ISAAC M. HELD, AND THOMAS L. DELWORTH

NOAA/Geophysical Fluid Dynamics Laboratory, Princeton, New Jersey

(Manuscript received 24 February 2000, in final form 1 August 2000)

ABSTRACT

The response of the Southern Hemisphere (SH), extratropical, atmospheric general circulation to transient, anthropogenic, greenhouse warming is investigated in a coupled climate model. The extratropical circulation response consists of a SH summer half-year poleward shift of the westerly jet and a year-round positive wind anomaly in the stratosphere and the tropical upper troposphere. Along with the poleward shift of the jet, there is a poleward shift of several related fields, including the belt of eddy momentum-flux convergence and the mean meridional overturning in the atmosphere and in the ocean. The tropospheric wind response projects strongly onto the model's ''Southern Annular Mode'' (also known as the ''Antarctic oscillation''), which is the leading pattern of variability of the extratropical zonal winds.

1. Introduction

In this report, we analyze the circulation changes simulated by the Geophysical Fluid Dynamics Laboratory (GFDL) Climate Dynamics Group's coupled general circulation model (GCM) in a series of transient global-warming ''scenario'' integrations. In these integrations, greenhouse-gas and sulfate-aerosol concentrations are gradually increased. We focus on the response of the zonal-mean Southern Hemisphere (SH) extratropical circulation for several reasons. First, since the SH circulation is largely zonally symmetric, it is practical to analyze the response within a relatively simple zonally symmetric dynamical framework. In addition, as we will discuss below, the model's SH extratropical circulation response is more robust than its Northern Hemisphere (NH) response, in the sense that it is similar among GFDL coupled models of varying resolution and among models from other institutions. Last, the SH focus has been stimulated by recent observational and modeling work in the climate-change context (Thompson and Wallace 1998, 2000; Fyfe et al. 1999; Thompson et al. 2000). This work suggests that the simulated response may be related to observed atmospheric circulation trends in the SH.

This study aims to describe the model's SH circulation response to greenhouse warming, as a prelude to an improved dynamical understanding of this response. After describing the model and the integrations performed (section 2), we present an overview of the SH coupled-model response (section 3). We then show how the wind response can be decomposed into a part that projects strongly onto the model's ''Southern Annular Mode'' (SAM) [see, e.g., Limpasuvan and Hartmann (1999) and Thompson and Wallace (2000)] and into a distinct, large-scale, response that extends from the model's tropical upper troposphere into the entire hemisphere's stratosphere (section 4). Last, we discuss whether these results are relevant to observed trends in the SAM and other open research issues (section 5).

2. Model description

We analyze output from the GFDL coupled atmosphere–ocean–land–ice model (Manabe et al. 1991; Manabe and Stouffer 1996; Haywood et al. 1997; Knutson et al. 1999). The atmospheric model uses finite differences in the vertical, with 14 vertical levels, and a σ (scaled pressure) coordinate defined by

$$\sigma = \frac{p}{p_s}, \tag{1}$$

where p is the pressure and p_s is the surface pressure. In the horizontal, the model uses the spectral transforms method, with R30 resolution, which utilizes a grid with approximately 2.25° lat × 3.75° long resolution. The global ocean model is the Modular Ocean Model (MOM1; Pacanowski et al. 1991), with 18 vertical levels and roughly 2° horizontal resolution. In order to reduce climate drifts, heat and salinity fluxes are adjusted by amounts that vary from season to season but not from year to year (Manabe et al. 1991). The flux adjustments are therefore independent of the state of the system. The

Corresponding author address: Geophysical Fluid Dynamics Laboratory, PO Box 308, Forrestal Campus, Princeton NJ 08542.
E-mail: pjk@noaa.gfdl.gov

circulation generated by the atmospheric component of this model, when integrated with prescribed climatological ocean surface temperatures, can be examined on the Internet at URL http://www.cdc.noaa.gov/gfdl.

All diagnostic calculations are performed on model σ levels. Those quantities referred to as ''surface'' quantities, for example, surface air temperature (SAT), are actually defined on the lowest model level, $\sigma = 0.997$. For display purposes, many quantities are plotted in pressure coordinates; the interpolation uses the σ-coordinate definition, Eq. (1), and the mean surface pressure.

We first analyze a 1000-yr-long control integration that starts when the atmosphere and ocean models are coupled. This integration has greenhouse-gas and sulfate-aerosol concentrations fixed at preindustrial levels. Although the integration undergoes some drift during the first century after coupling, it undergoes very little drift for the remaining 900 years. The zonal-mean, annual-mean SAT cools by at most 0.06 K century^{-1}, for years 101–1000. The zonal-mean, annual-mean surface winds drift by less than 0.02 m s^{-1} century^{-1} for the same time period. The largest trends in the SAT and winds occur at high latitudes. The areal extent of SH sea ice is generally well simulated by this model, although sea ice is generally too thick near the coast of Antarctica. After an approximately 10% increase in the first 100 yr of the coupled integration, the total volume of sea ice poleward of 40°S has no trend over the last 900 yr of the coupled integration.

Most of the diagnostics shown in this study use the last 800 yr (i.e., yr 201–1000) of the control integration. Daily snapshots of spectral-component data that are required to calculate atmospheric transient-eddy statistics are taken from years 111–225 of the control integration. The SAM regression maps discussed in section 4 also use this segment.

We also analyze an ensemble of three 225-yr-long ''scenario'' integrations that branch off the control integration at well-separated intervals (years 116, 351, and 401 of the control integration). The scenario integrations have greenhouse-gas and sulfate aerosol concentrations that increase with time, according to the IPCC IS92a scenario (Mitchell et al. 1995; Haywood et al. 1997), from 1865 to 2089. Most of the diagnostics shown here use all three scenario members. Daily snapshot data from a single scenario realization have been used to calculate transient-eddy statistics. Since the mean response is similar in all three realizations, we expect the transient-eddy response from this single realization to sample adequately the ensemble.

3. Description of the SH circulation response

Figure 1 shows the zonal-, ensemble-, and annual-mean SAT anomaly of the scenario ensemble with respect to the control integration, as a function of time and latitude, for the period 1865–2089. In the figure, annual means are computed first, and a 5-yr running mean is then applied. The NH warms more quickly than the SH: by the end of the run (years 2085–89), the NH has warmed approximately 5.2 K, while the SH has warmed approximately 3.4 K. Besides the contrast in the mean warming in each hemisphere, there is also a significant contrast between the warming patterns. The NH warming generally increases toward the pole. The SH warming, on the other hand, decreases from the Tropics towards a minimum in the latitude band 55°–65°S, and increases poleward of these latitudes.

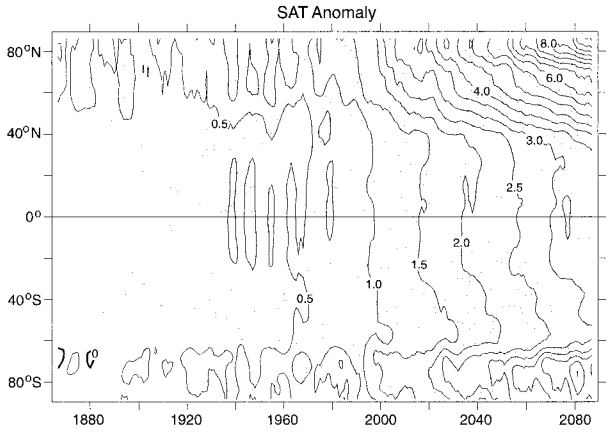

FIG. 1. Contours: Time series of the ensemble-, annual-, and zonal-mean SAT of the scenario integrations minus the 800-yr time- and zonal-mean SAT of the control integration. A 5-yr running mean has been applied to the data. Contour interval: 0.5°C. Shading denotes regions where the magnitude of the anomaly is greater than $2\sigma_{ctl}$.

This contrast in the simulated thermal response between the two hemispheres is robust and well-known from previous studies. Bryan et al. (1988) first identified the interhemispheric asymmetry in the warming in transient greenhouse-gas-increase integrations of a model with sector-ocean geometry, and the same kind of warming pattern is found in other models [see, e.g., Kattenberg et al. (1996), Dai et al. (2001)]. The poleward amplification of the signal in the NH and the high SH latitudes can be attributed to snow- and sea-ice-albedo feedbacks that strengthen toward higher latitudes.

The minimum in warming in the latitude band 55°–65°S can be attributed to the thermal inertia associated with the deep-ocean mixing of heat in the SH (Manabe et al. 1991). It has been suggested that this mixing may be too strong, owing to the current ocean model's isopycnal diffusion scheme, in comparison with models that use oceanic mesoscale eddy parameterizations that diffuse isopycnal thickness (England 1995). However, the greenhouse-warming integrations of the National Center for Atmospheric Research Climate System Model (NCAR CSM; Dai et al. 2001), which is a coupled climate model whose ocean component uses the Gent and McWilliams (1990) thickness-diffusing scheme, also produce a minimum in SH extratropical ocean surface warming. We conclude that the simulated minimum

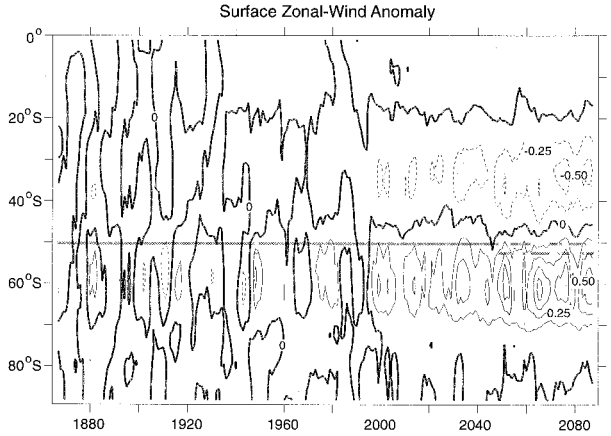

FIG. 2. As in Fig. 1, but for the surface zonal wind. Contour interval: 0.25 m s^{-1}. The × symbols indicate the latitude, on the model grid, of the jet maximum, after the winds have been filtered by a 5-yr running mean.

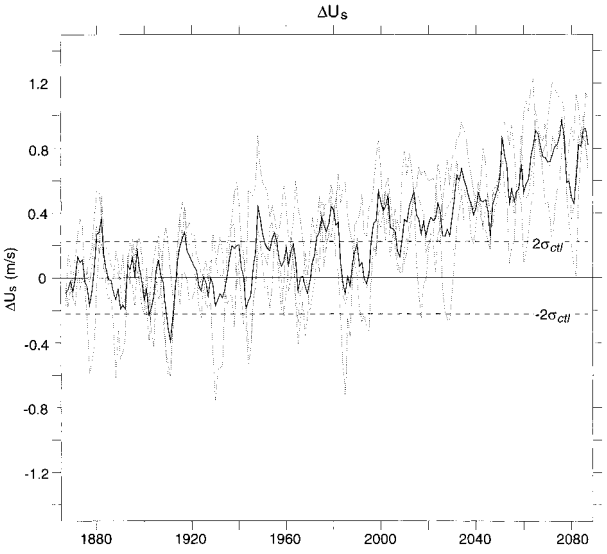

FIG. 3. The scenario-integration anomaly of the index ΔU_s defined in Eq. (2). Solid: ensemble mean. Dotted: individual realizations. Horizontal lines: $2\sigma_{\text{ctl}}$ for ΔU_s.

in warming over the Southern Ocean latitudes is physically plausible and does not appear to be an artifact of the mixing scheme employed.

In Fig. 1, shading is applied where the magnitude of the ensemble-mean SAT anomaly is greater than a measure of the control-run variability. This measure is twice the standard deviation of the annual-mean control-run time series ("$2\sigma_{\text{ctl}}$"), after the time series has been filtered by the 5-yr running mean, at each latitude. The magnitude of the response exceeds and remains greater than $2\sigma_{\text{ctl}}$ as early as the decade 1911–20 in the SH subtropics, where the interannual variability is relatively weak. By the decade 1991–2000, the warming exceeds $2\sigma_{\text{ctl}}$ at all latitudes.

Figure 2 is similar to Fig. 1, but applies to the SH surface zonal wind anomalies. The dominant pattern is a positive anomaly poleward of 45°S and a negative anomaly between 45° and 20°S, with an amplitude of about 1 m s^{-1} toward the end of the run. The shading relates to the $2\sigma_{\text{ctl}}$ threshhold, as in Fig. 1. We see that at a given latitude, the magnitude of the surface zonal wind response does not exceed and remain greater than the $2\sigma_{\text{ctl}}$ threshhold until the decade 2051–60, much later than for the SAT response. However, the pattern of the anomaly is established as early as the decade 2001–10. This is demonstrated more clearly in Fig. 3, which plots the time series of an index that has been constructed to pick out the dipole pattern in Fig. 2. The quantity plotted is the anomaly, with respect to the control integration, of

$$\Delta U_s = \langle U_s \rangle_{70°\text{S to }45°\text{S}} - \langle U_s \rangle_{45°\text{S to }20°\text{S}}. \qquad (2)$$

In Eq. (2), U_s is the surface zonal wind and the angle brackets represent a horizontal spatial mean over the latitude bands indicated in the subscripts. The positive bias in this index becomes evident by the decade 1951–60; it crosses the $2\sigma_{\text{ctl}}$ threshold decisively by the decade 2011–20.

Figure 4 shows the seasonal dependence of the control-integration zonal wind and of the zonal-wind response, at the surface and at 250 mb, for the SH. The response is defined as the 2065–89 ensemble- and time-mean of the scenario integrations minus the 800-yr time mean of the control integration. The figure shows that the dipole response extends into the extratropical upper troposphere and consists of a poleward shift of the main jet. The surface response (Fig. 4b) has a weak seasonal cycle, with a minimum in the SH late winter and early spring. The upper-tropospheric extratropical wind response (Fig. 4d) has a stronger seasonal dependence, being strongest in the summer half-year, when the jet is farthest poleward. Figure 4d shows that the tropical upper-tropospheric response consists of a positive anomaly throughout most of the year. For the model lower stratosphere (not shown), this positive anomaly extends throughout the hemisphere for all months.

We now focus on the extratropical circulation response for the months November–February (NDJF), for which the dipole pattern is strongest throughout the troposphere. The vertical–meridional profile of the control-run zonal-mean zonal wind for these months is shown in Fig. 5a and the response is shown in Fig. 5b. The zonal wind response described in the preceding figures is a deep equivalent-barotropic structure that amplifies into the upper troposphere. Capping this pattern is the less seasonally dependent positive wind anomaly. Figures 5c–d relate to the SAM and will be discussed in section 4.

What, precisely, do we mean when we characterize the tropospheric SH summertime wind response as a poleward shift? If, at a given pressure level, the control-integration zonal-mean zonal-wind profile, $U = U(y, p)$, where y is the meridional coordinate, shifts, without

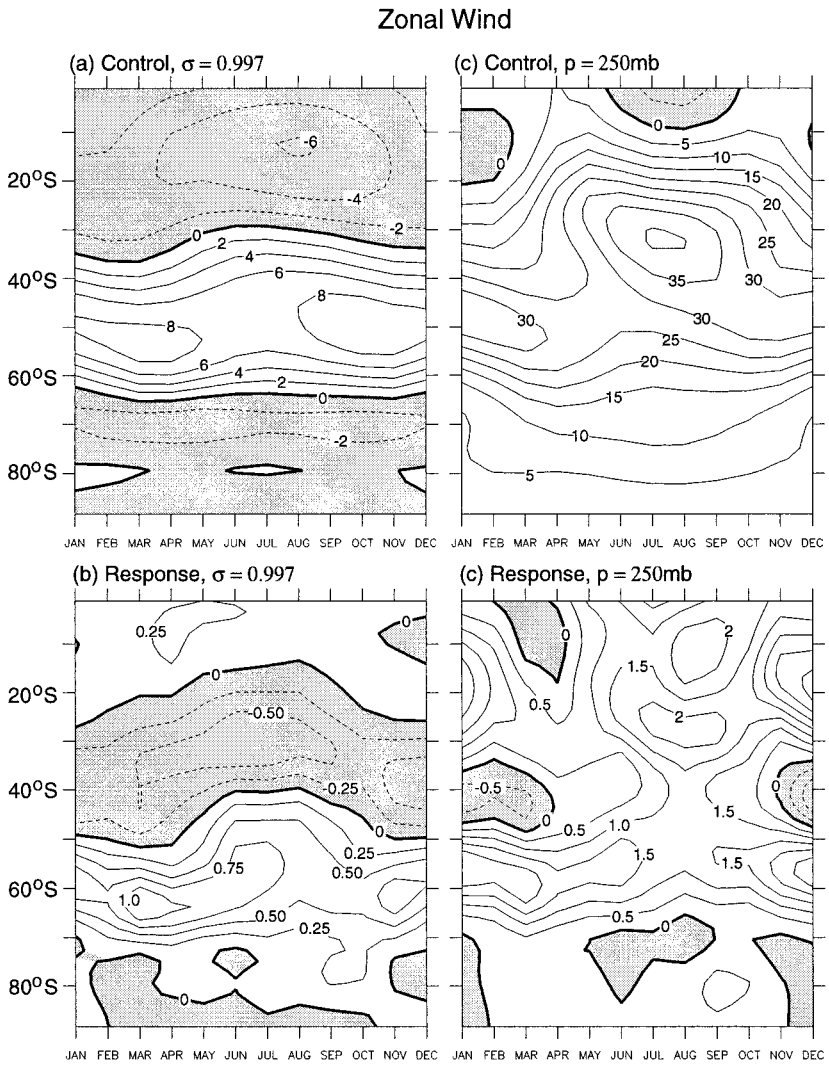

FIG. 4. The seasonal cycle of the climatological surface zonal-mean zonal wind for (a) the 800-yr time mean of the control integration, and (b) the ensemble mean response, years 2065–89. (c), (d) As in (a) and (b), but at 250 mb. Shading and dashed contours indicate negative values. Contour interval: (a) 2 m s^{-1}; (b) 0.25 m s^{-1}; (c) 5 m s^{-1}; (d): 0.5 m s^{-1}.

changing shape, by a meridional distance δy, then the change in the wind δU is

$$\delta U = U(y - \delta y, p) - U(y, p) \approx -\delta y \frac{\partial U}{\partial y}. \quad (3)$$

In Eq. (3), the approximation follows for displacements δy that are small when compared with the scale of variation of the jet. Suppose, instead of using Eq. (3), that we estimate the wind response by

$$\delta \hat{U} = -\delta \hat{y} \frac{\partial U}{\partial y} + c_1. \quad (4)$$

In Eq. (4), $\delta \hat{U}$ is the estimate of δU and is assumed to be linearly related to the control-integration $-\partial U/\partial y$, using an estimated linear-regression coefficient $\delta \hat{y}$ and an estimated intercept c_1. If the resulting sample correlation coefficient r^2 were close to unity and the constant c_1 were small in comparison with the characteristic amplitude of δU, the description, represented by Eq. (3), of the wind response as a shift would be appropriate.

We calculate the linear least squares estimate [Eq. (4)] for the surface zonal-mean zonal-wind response and find that Eq. (3) is indeed an appropriate description. In order to match the extratropical wind response pattern, no cosine-of-latitude weighting has been used in the estimate. The estimate yields $\delta \hat{y} = -0.82°$ latitude, which corresponds to a southward shift of about 0.8° latitude. The correlation between the response δU and the meridional wind shear $\partial U/\partial y$ is strong, with $r^2 = 0.95$. The intercept, $c_1 = 0.06$ m s^{-1}, is small in comparison with the characteristic strength of the anomaly, which is about 0.8 m s^{-1}. The estimate is shown in Fig.

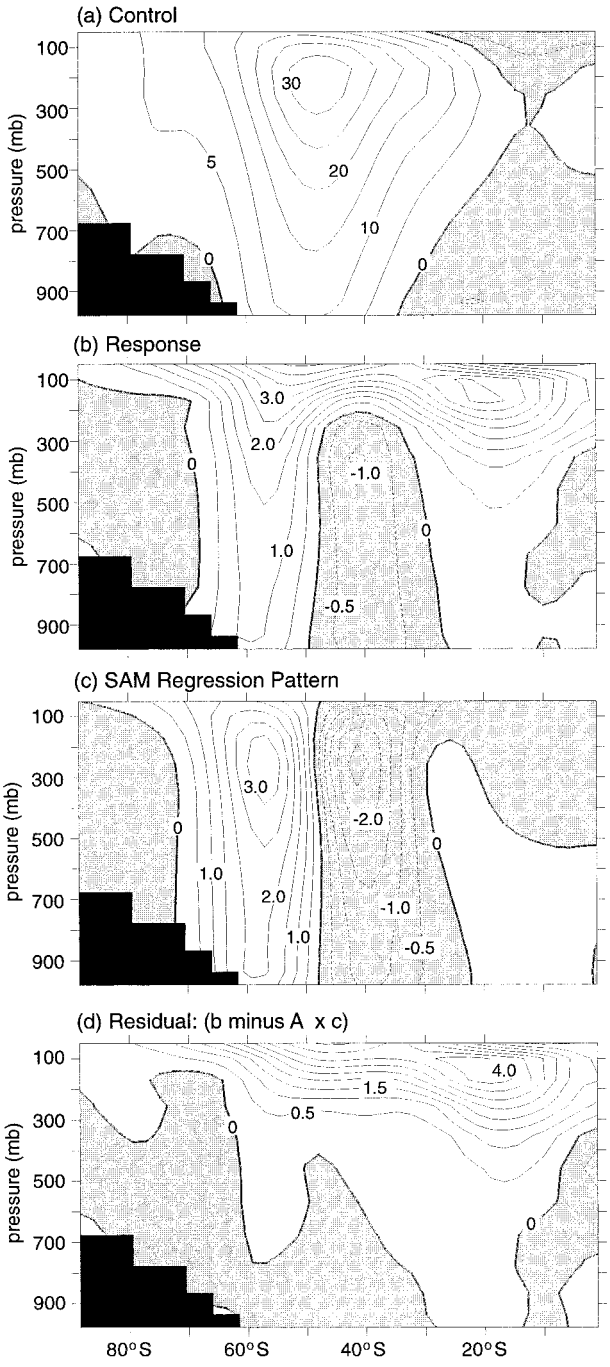

FIG. 5. (a) Zonal- and NDJF-mean climatological zonal wind for the control integration. Contour interval: 5 m s^{-1}. (b) As in (a), for the ensemble-mean response, years 2065–89. (c) As described in section 4, the regression map of the zonal-mean zonal wind for the SLP-based SAM index defined for NDJF. (d) As described in section 4, the residual remaining once the SAM pattern in (b) has been removed from the response pattern in (b). Contour interval in (b)–(d): 0.5 m s^{-1}. Shading and dashed contours indicate negative values. Black masking for grid boxes with $p < p_s$.

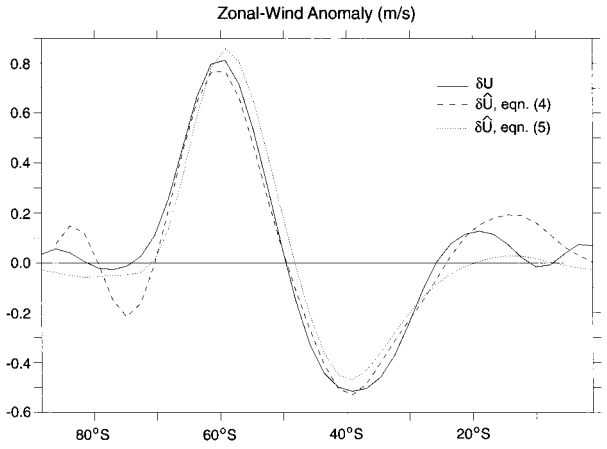

FIG. 6. Solid: ensemble-, NDJF-, and zonal-mean surface zonal-wind response, years 2065–89 (m s^{-1}). Dashed: $\delta\hat{U}$, from Eq. (4). Dotted: As discussed in section 4, $\delta\hat{U}$ from Eq. (5).

6 (dashed), and compares well with the wind response (solid). The dotted curve in Fig. 6 relates to the SAM and will be discussed in section 4.

Equation (3) indicates that two distinct meridional length scales are involved in the wind response. The first, $|\delta y|$, is the scale of the meridional displacement of the jet. We have found this scale to be about 0.8° latitude, which is less than one-third of the roughly 2.5°-latitude resolution of the model. How the jet displacement occurs in the transient integration is made explicit by the × symbols in Fig. 2, which show the latitude, on the R30 grid, of the maximum surface winds for the 5-yr running-mean time series. We see that as the scenario integration proceeds, the jet maximum occasionally shifts one latitude row poleward of its original position. The quantity $\delta\hat{y} = 0.82°$ latitude represents the average of this behavior over the last 25 yr of the integration.

From Eq. (3), the second length scale that characterizes the response is the length scale of variation of the wind shear $\partial U/\partial y$. From the dashed curve in Fig. 6, we see that this scale of variation is about 40° latitude and is similar to the scale of the jet itself. The wind shear scale is much larger than the meridional displacement scale, $|\delta y| \simeq 0.8°$ latitude; this justifies the approximation in Eq. (3). It is this larger wind-shear scale that characterizes the wind anomaly in Figs. 2 and 4. Therefore, the model is able to resolve the response, even though the jet is only slightly displaced.

The SH extratropical tropospheric circulation response is robust in the sense that it is similar in every transient greenhouse-warming integration we have performed at both R30 and R15 resolutions, and is found, in addition, in coupled models from other modeling groups [e.g., the Canadian Climate Centre for Modeling and Analysis (CCCma) coupled model (Fyfe et al. 1999); and the NCAR CSM (see Dai et al. 2001, Fig. 37)]. The NH circulation response is quite different from

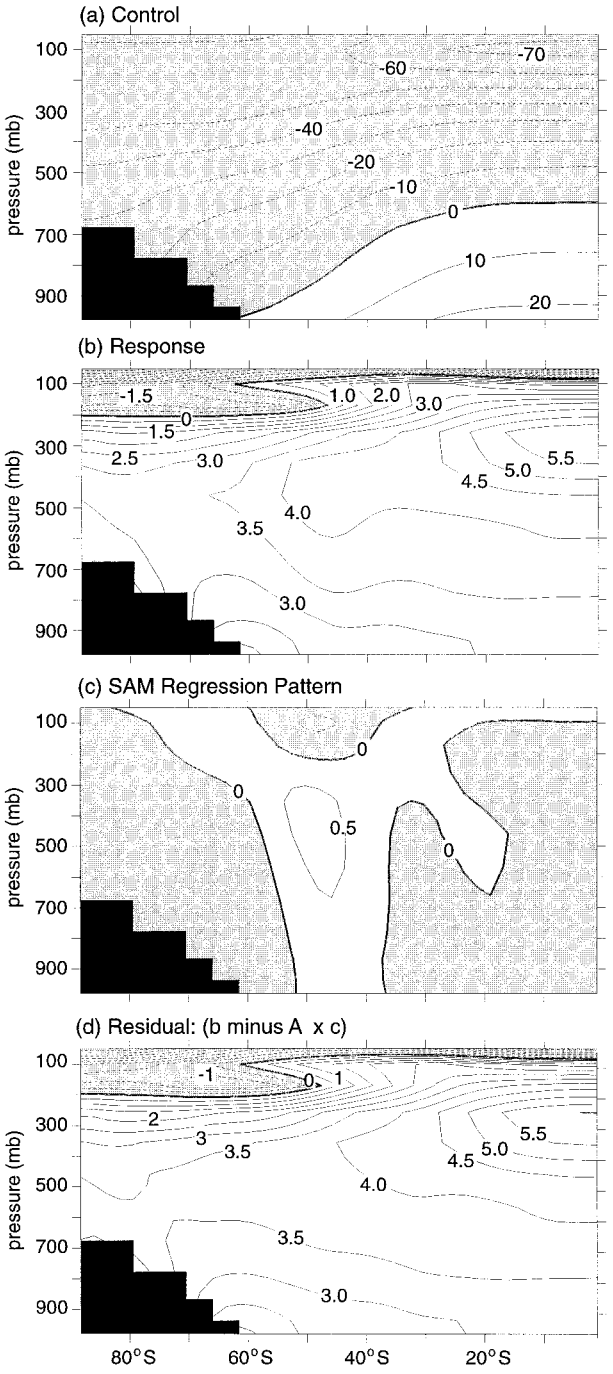

FIG. 7. As in Fig. 5, for the temperature. Contour interval (a): 10°C; (b)–(d): 0.5°C.

the SH response and not as robust. In both the R15 and R30 resolution integrations, the NH zonal wind response (not shown) consists of a seasonally independent positive anomaly equatorward of 40°N and a negative anomaly poleward of this latitude, and it cannot be described as a simple shift of the circulation. The NH circulation response varies among modeling groups. We will return to this point below.

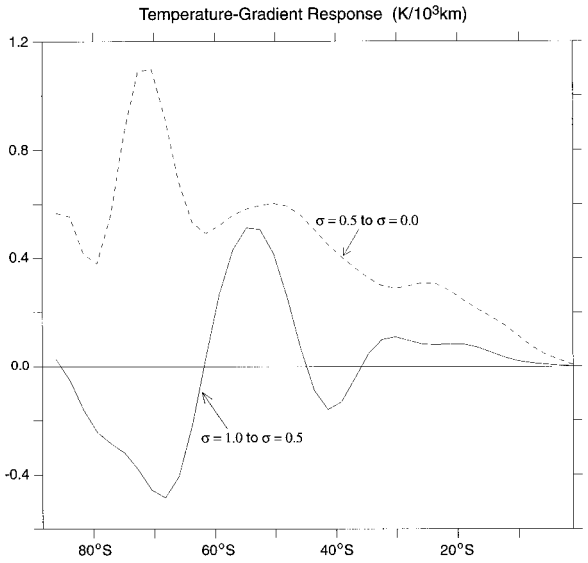

FIG. 8. The vertical- and ensemble-mean meridional temperature gradient response for years 2065–89, averaged over the lower half of the model ($1.0 \leq \sigma < 0.5$, solid) [°C (1000 km)$^{-1}$] and over the upper half of the model ($0.5 \leq \sigma < 0$, dashed).

Figures 7, 8, and 9 show various aspects of the SH thermal response. From the zonal-mean temperature response in Fig. 7b, we see that the basic features of the surface thermal response—the minimum in warming over the Southern Ocean latitudes and the high-latitude maximum at the higher latitudes—extend into the lower troposphere. The accompanying meridional temperature-gradient response consists of alternating bands of enhanced and weakened temperature gradients. This is shown by the solid curve in Fig. 8, which plots the zonal-mean meridional temperature-gradient response, averaged in the vertical between $\sigma = 1.0$ and $\sigma = 0.5$. This response pattern is robust, since it is present in every scenario realization.

At upper levels, the temperature response in Fig. 7b has other features that are familiar from previous greenhouse-warming integrations [e.g., Mitchell et al. (1990), Fig. 5.2]. These include the maximum in warming in the tropical upper troposphere associated with a shift of the tropical temperature profile to a warmer moist adiabat and the stratospheric cooling associated with enhanced CO_2 concentrations. Accompanying these changes is an overall positive meridional temperature gradient anomaly (Fig. 8, dashed curve) and an upward shift of the static stability profile (Fig. 9) in the upper half of the model. A linear regression estimate, similar to that used in Eq. (4), shows that this upward shift is roughly 10 mb in the subtropics and 20–30 mb in the extratropics (details of the calculation omitted). As was the case for the meridional shift of the jet, the model is capable of resolving the static-stability anomaly because its scale is much larger than the 10–30 mb scale of the shift of the static-stability profile.

The upward shift of the upper tropospheric static sta-

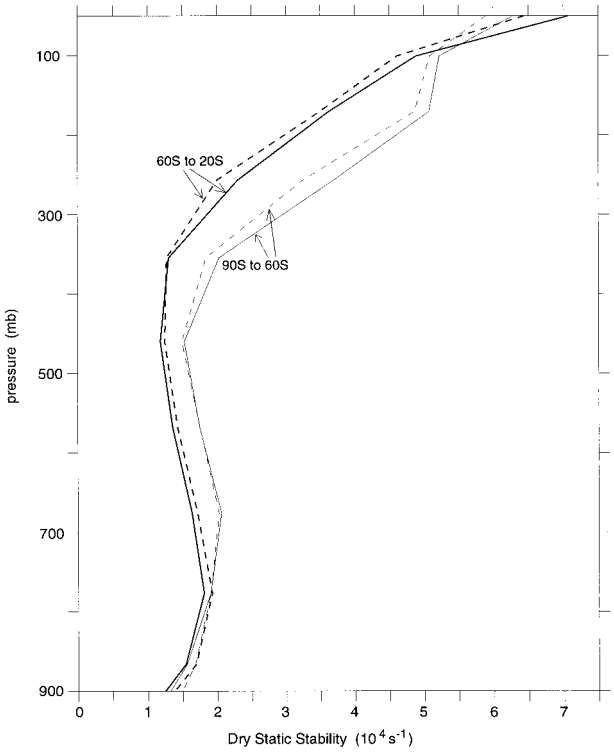

FIG. 9. The dry static stability for the control run averaged over latitudes 60°–20°S (solid, thick) and 90°–60°S (solid, thin) and for the ensemble-mean scenario integration, years 2065–89, averaged over 60°–20°S (dashed, thick) and 90°–60°S (dashed, thin).

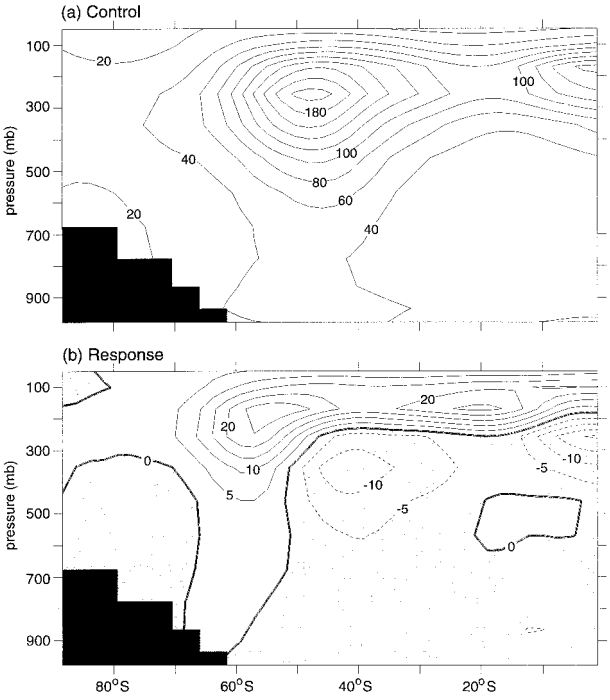

FIG. 10. (a) Control and (b) response for NDJF eddy kinetic energy. Contour interval: (a) 20 m^2 s^{-2} and (b) 5 m^2 s^{-2}. This figure uses daily snapshot data from a shorter segment of the control run and a single scenario realization, as discussed in section 2.

bility profile, shown in Fig. 9, implies that greenhouse warming has the effect of increasing the depth of the troposphere. Accompanying this basic change to the stratification is an upward shift of the transient-eddy activity. This is demonstrated in Fig. 10, which shows the control-run eddy kinetic energy per unit mass and the warming response of this field. There is a broad upper-level upward shift of the eddy kinetic energy maximum, as well as a poleward shift of the main band of eddy activity in the extratropics.

The surface-wind change shown by the solid curve in Fig. 2 is directly linked to changes in the eddy momentum flux. By a vertical-, time-, and zonal-mean momentum balance, the mean momentum flux convergence must balance the zonal-mean surface wind stress. In the midlatitudes, the momentum-flux convergence arises primarily from the eddies. We therefore expect that a poleward shift in the surface jet will be accompanied by a poleward shift of the band of eddy momentum flux convergence that maintains the jet. This expectation is supported by the control eddy momentum-flux convergence and the response in Figs. 11a and b. There is a poleward shift of the dominant band of momentum-flux convergence. At upper levels, equatorward of 50°S, there is also evidence of an upward shift of the momentum flux convergence that is consistent with the raising of the tropopause seen in Figs. 9 and 10b.

Although the eddy momentum flux response is linked to the wind response, the eddy sensible heat flux response is more closely linked to the temperature response. We find, especially in the free lower troposphere, that much of the extratropical eddy sensible heat flux response is diffusive, that is, down the perturbed temperature gradient. This is evident in Fig. 12, which shows the 850-mb meridional temperature-gradient response (solid) for one of the scenario realizations and the 850-mb meridional sensible heat flux response for that realization. Both quantities have been multiplied by the cosine of latitude. The simple diffusive picture breaks down at lower latitudes, perhaps because of moist effects.

The changes to the atmospheric surface winds are linked to changes in the atmospheric and oceanic wind-driven circulation in an expected way. Figure 13a plots the zonal-mean surface meridional wind (solid), the zonal-mean surface meridional ocean currents (dashed), and the zonal-mean surface zonal wind stress (dotted). Figure 13b plots the response for these quantities. The Ferrel cell in the atmosphere and the wind-driven overturning in the ocean both shift poleward with the wind stress. Similar circulation changes have been documented in Bryan et al. (1988) and Manabe et al. (1991).

4. Projection of response onto internal variability

In this section, we show that the model SH extratropical wind response is similar to the dominant pattern

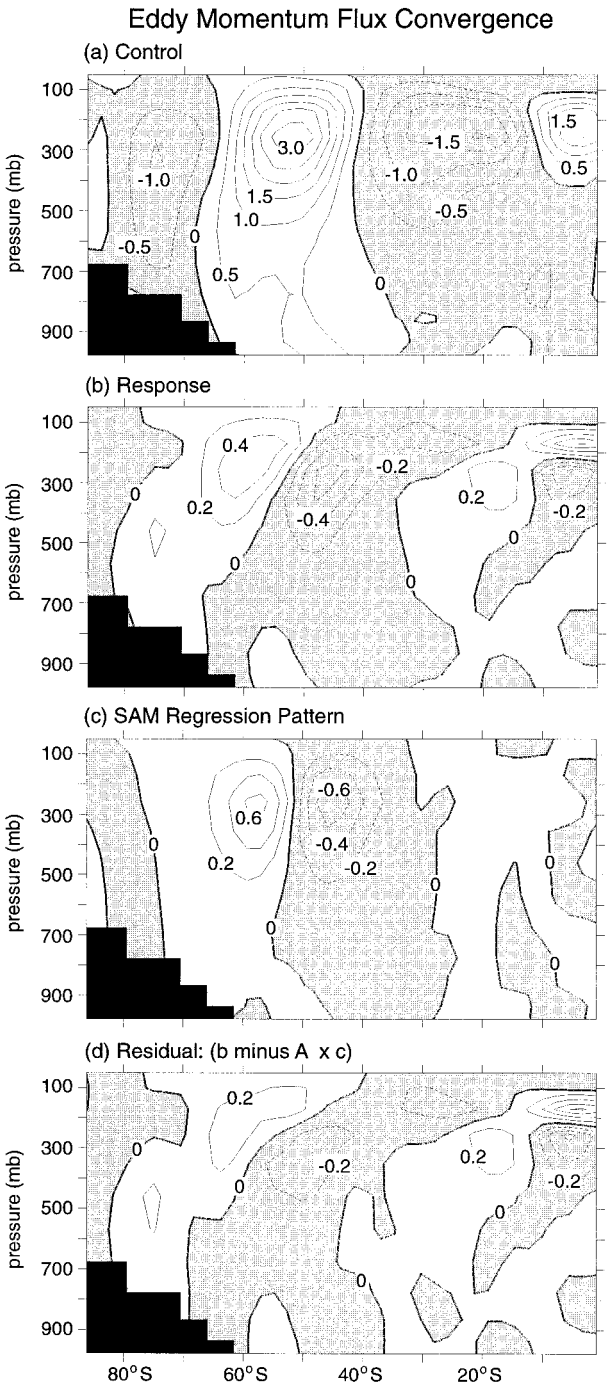

FIG. 11. As in Fig. 5, for the horizontal eddy momentum flux convergence per unit mass. Contour interval: (a) 0.5 m s^{-1} day^{-1}; (b)–(d) 0.2 m s^{-1} day^{-1}. This figure uses daily snapshot data from a shorter segment of the control run and a single scenario realization, as discussed in section 2.

of variability of the SH extratropical wind. This pattern of variability consists of an equivalent barotropic dipole with its node located at the mean jet maximum. The pattern characterizes the vacillation of the SH hemisphere zonal winds both on interannual and intraseasonal timescales and has been documented in observations, in atmospheric GCM simulations, and in coupled-model simulations [e.g., Yu and Hartmann (1993), Hartmann and Lo (1998), Fyfe et al. (1999), Limpasuvan and Hartmann (1999), Thompson and Wallace (2000)]. Following Limpasuvan and Hartmann (1999), we use the name ''Southern Annular Mode'' to refer to

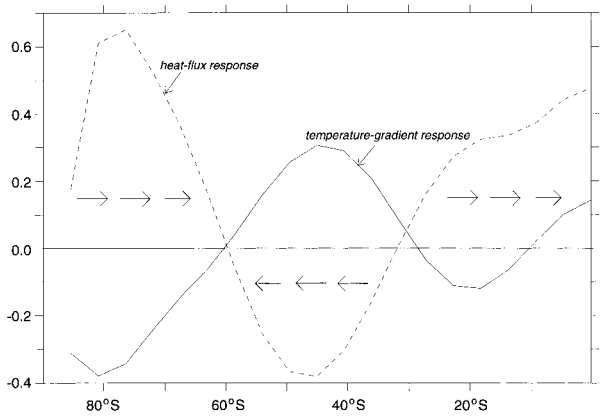

FIG. 12. Solid: 850-mb meridional temperature-gradient response [°C (1000 km)$^{-1}$] for a single scenario realization. Dashed: 850-mb meridional heat-flux response (°C m s^{-1}) for the same realization. Both curves are multiplied by the cosine of the latitude. Arrows indicate the direction of the heat-flux response. These quantities are not defined poleward of 73°S, where $p_s < 850$ mb.

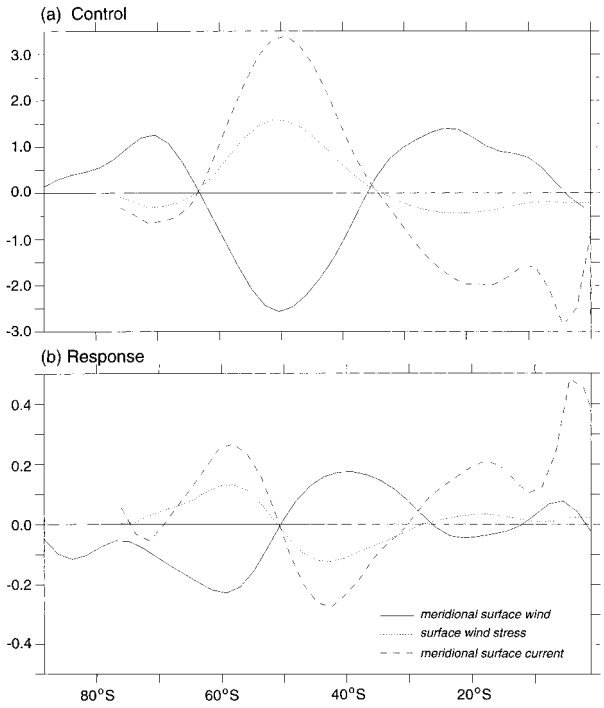

FIG. 13. (a) Surface zonal-mean meridional wind (m s^{-1}; solid), 100 times the surface zonal-mean meridional ocean current (m s^{-1}; dashed) and 10 times the surface zonal wind stress (Pa; dotted), for the control integration. (b) As in (a), for the ensemble-mean response, years 2065–89.

this zonal-wind vacillation pattern, and the term ''Northern Annular Mode'' (NAM) to refer to its NH counterpart The NAM is often called the ''Arctic oscillation'' (NAM) and the SAM, the ''Antarctic oscillation'' (AAO) (e.g., Fyfe et al. 1999; Thompson and Wallace 2000).

Thompson and Wallace (2000) and Thompson et al. (2000) argue that the NAM and SAM are dynamically similar, that there have been recent trends in these patterns, and that these trends might be the result of anthropogenic climate change. The modeling studies of Shindell et al. (1999) and Fyfe et al. (1999) lend some support to these claims. The issue is confused, however, by the variation, mentioned in section 3, of the NH greenhouse-warming response among different models. In the Shindell et al. (1999) study, a NAM trend dominates the extratropical greenhouse-warming signal, but only for simulations with enhanced resolution in the stratosphere. In the Fyfe et al. (1999) study, which uses a model with relatively coarse resolution in the stratosphere, trends in the NAM and SAM also emerge under greenhouse warming. The NAM trends identified by Fyfe et al. (1999), however, account for far less of the simulated surface-pressure response than the NAM trends found by Shindell et al. (1999) [see Shindell et al. (2001) for further discussion]. In the GFDL greenhouse-warming integrations, which are of comparable resolution to the Fyfe et al. (1999) integrations, there are no NAM trends.

We define the SAM as the leading empirical orthogonal function (EOF) of variability of the sea level pressure (SLP) southward of 20°S. The SAM pattern is insensitive to this definition, and other fields, such as the 850-mb geopotential height or the extratropical zonal winds, may be used (Thompson and Wallace 2000). The EOFs are calculated from monthly mean time series in which the annual cycle has been removed. Typically, a subset of calendar months is selected. We define an SAM index that is the principal-component time series associated with this EOF, with a standard deviation of unity. We present ''regression maps'' that plot the covariance of this SAM index with the time series of other fields. For the calculations presented here, the SAM is defined as the leading EOF in SLP for NDJF for years 111–225 of the control. It accounts for 26% of the variance, which is an amount comparable to that of the observed SAM EOF for the SH summer season (Thompson and Wallace 2000). The SAM EOF is well separated from the next EOF, which accounts for 17% of the variance.

Limpasuvan and Hartmann (1999) show that the atmospheric component of this model, integrated with prescribed sea surface temperatures that vary seasonally but that do not vary from year to year, reproduces the main features of the observed SAM quite closely, including its structure and the amount of variance it explains. This conclusion also holds for the coupled model, implying that the ocean coupling has little to do with the spatial pattern of the SAM itself. The model does less well at capturing the observed upper-level seasonal cycle of the SAM. In particular, the stratospheric and upper-tropospheric amplitudes of the pattern are too weak in the ''active'' seasons identified by Thompson and Wallace (2000). This is probably the result of a poorly resolved stratosphere in this climate model.

The relationship between the spatial patterns of the response to warming and of the SAM is straightforward to demonstrate. Figure 5c shows the SAM regression map for the control-run zonal-mean zonal wind, for the months NDJF. By convention, this wind pattern corresponds to the positive phase of the SAM. The similarity between the tropospheric anomalies in Figs. 5b and 5c is quite apparent. Similar features include the equivalent barotropic character of the dipole and the amplification of the anomaly with height.

Figure 5d is a residual plot that shows the response with the SAM pattern removed. This figure is obtained as follows: the wind response (Fig. 5b) at the surface is fit by means of a linear regression onto the SAM pattern (Fig. 5c) at the surface, between the latitudes 90°S and 20°S. The least squares estimate $\delta\hat{U}$ in this case is

$$\delta\hat{U} = A\delta U_{\mathrm{SAM}} + c_2, \tag{5}$$

which should be compared with Eq. (4). Here, $\delta\hat{U}$ is assumed to be linearly related to the control integration SAM surface-wind anomaly δU_{SAM}, using an estimated linear-regression coefficient A and an estimated intercept c_2. This yields a regression coefficient of $A = +0.54$, and a small offset of $c_2 = -0.03$ m s^{-1}. The positive sign of A indicates that the warming pattern projects onto the positive phase of the SAM and the magnitude indicates that the climate-change signal is about one-half of the SAM variability. The correlation coefficient $r^2 = 0.94$ indicates that the surface-wind response and the surface-SAM signature are highly correlated. The result of the least squares fit of the SAM onto the surface-wind response is shown by the dotted curve in Fig. 6. It is close to the response and to the linear fit to the shear $-\partial U/\partial y$ discussed in section 3. Figure 5d is the result of subtracting the SAM pattern in Fig. 5c, multiplied by $A = +0.54$, from Fig. 5b. The result is a smooth, large-scale pattern with little tropospheric structure and a strong westerly wind anomaly in the stratosphere and in the tropical upper troposphere. The residual near the surface is particularly weak, consistent with the small value of $c_2 = -0.03$ m s^{-1}.

Figures 5b–d imply that the tropospheric response to global warming can be decomposed into two distinct patterns, an SAM-like pattern that emerges most strongly in the SH summer half year and a westerly wind anomaly that extends from the tropical upper troposphere into the entire hemisphere's stratosphere. The three curves in Fig. 6 imply, in turn, that both the response to warming and the SAM itself involve simple shifts of the jet, largely without a change in shape. The

jet-position variability, which includes both intraseasonal and interannual timescales, has a characteristic amplitude of 2° latitude; the model response for the years 2065–89 is roughly one-half of this.

Figures 11c,d are similar to Figs. 5c,d, but for the eddy momentum flux convergence. Figure 11c shows the control-run eddy momentum-flux convergence SAM regression. Similar results were found by Limpasuvan and Hartmann (1999). Figure 11d shows the result of subtracting Fig. 11c, multiplied by the regression coefficient $A = +0.54$ obtained in Eq. (5), from Fig. 11b. The SAM signature in the eddy momentum flux convergence accounts for much of the poleward shift of the eddy momentum flux convergence region in the latitude band from 65° to 45°S in Fig. 11b. The residual is a vertically oriented dipole pattern whose vertical integral is relatively small. This is consistent with the relatively weak surface response evident in Fig. 5d, and with the small value of $c_2 = -0.03$ m s^{-1} obtained from Eq. (5). The vertical dipole structure is also consistent with the deepening of the troposphere discussed in section 3.

Although the zonal-wind and eddy-momentum-flux convergence response projects strongly onto the SAM, the situation is different for the thermal response. Figure 7c shows that the zonal-mean thermal anomaly associated with the SAM is relatively weak, with a maximum amplitude of approximately 0.5 K in the middle troposphere. Removing the SAM pattern from the warming pattern, with the same regression coefficient, $A = +0.54$, as before, leaves the warming pattern largely unchanged (Fig. 7c). The largest change occurs in the middle troposphere, where some of the smaller-scale, extratropical features, pointed out in the discussion of Fig. 7b, are removed. The SAM also has a weak eddy heat flux component that projects minimally onto the global warming response (figure not shown). We conclude that the thermal signature of the SAM accounts for very little of the zonal-mean thermal response to global warming, particularly the near-surface and upper-level warming.

The GFDL model results are consistent with those of Fyfe et al. (1999), who find positive SAM index trends in scenario runs of the CCCma coupled model. However, as we will discuss below, the simulated trends in the GFDL model are too weak to represent unambiguously the SAM observed trends.

5. Discussion

We present the following preliminary dynamical interpretation of the SH circulation response to warming, based on the results of sections 3 and 4. First, we observe that the poleward shift of the circulation is strongest in SH summer, when the SH jet is farthest poleward and relatively well separated from the Hadley cell. During this time, the jet can be considered to be ''eddy driven,'' that is, in balance with baroclinic eddy driving. Therefore, the zonal-mean wind response must be predominantly balanced by the baroclinic eddy driving response, in the way illustrated in Fig. 11b.

Next, we note that in the control simulation and in the observations, the dominance of the SAM indicates that the main mode of variability of the jet is to shift poleward and equatorward rather than to change shape or strength. This mode of variability must be balanced by variability in the eddy forcing, in the way illustrated in Fig. 11c. Although this is the dominant mode of variability, other modes of eddy-driven jet variability are easy to find. For example, the second EOF of variability of the zonal wind, both in this model (not shown) and in the observed SH general circulation (D. Lorenz and D. Hartmann 2000, personal communication) has a structure that weakens the jet core and strengthens the jet flanks in one phase and vice versa in the opposite phase.

We only partially understand why the primary mode of eddy-driven jet variability involves jet displacements. From the point of view of studies of baroclinic turbulence (e.g., Rhines 1975; Panetta 1993; Lee 1997), it is well known that long-lived jets of a relatively small meridional scale tend to emerge within relatively broad baroclinic regions. Once they emerge, they are only weakly constrained to stay at any particular latitude, and their meridional position varies considerably. Because of the overlap between the SH baroclinic zone and jet scales, it is unclear how directly these ideas apply to the SH circulation. Nevertheless, the fact that the SAM is the dominant mode of variability does suggest that the jet position is more weakly constrained than, for example, the jet shape or strength.

In the perturbed climate, direct radiative, moisture, and ice albedo effects change the thermal environment in the SH. The direct response consists of a tropical upper tropospheric warming, stratospheric cooling, a relatively weak near-surface warming over the Southern Ocean, a stronger warming at high latitudes, and a deepening of the troposphere. The direct response in the stratosphere and tropical upper troposphere has a relatively weak seasonal cycle and is associated with a positive anomaly in the SH pole-to-equator temperature gradient. This temperature-gradient response is, in turn, associated with a positive wind anomaly in the model stratosphere and tropical upper troposphere.

The large-scale direct response does little to alter the strength and shape of the tropospheric jet, but merely shifts its position poleward by less than 1° latitude. This suggests that, as for the internal variability, the jet shape and strength are more strongly constrained in response to external forcing than the jet position. The circulation changes, as it were, along the path of least resistance. These remarks do not answer the question of what determines the direction or magnitude of the shift of the jet, but are meant to provide a starting point for understanding why the response involves first and foremost a shift.

Although these integrations produce an SAM-like cir-

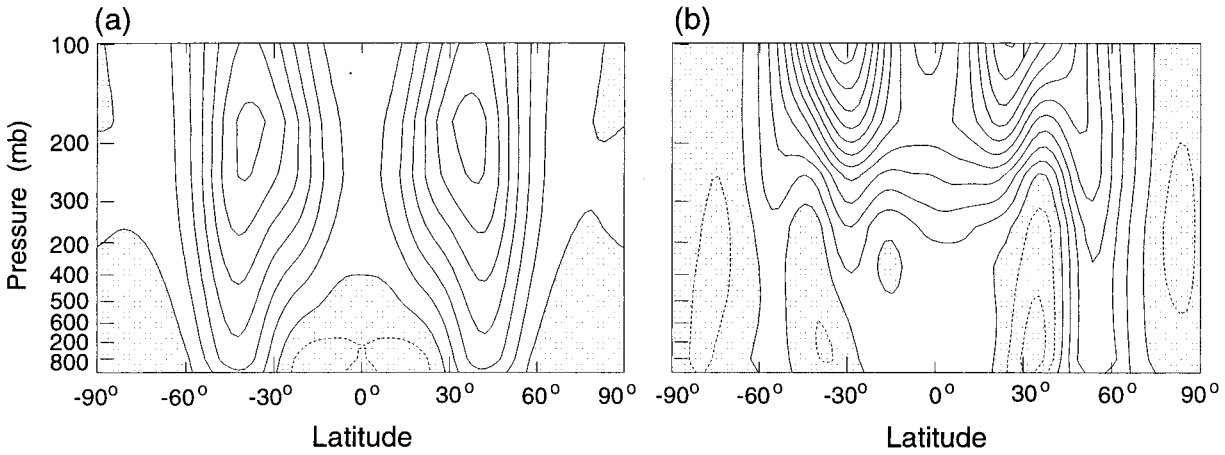

FIG. 14. (a) Zonal-mean zonal wind for the control integration of an idealized zonally symmetric ''aquaplanet'' model. (b) The response for the case in which the ocean surface temperatures are increased uniformly by 3 K. Contour interval: (a) 5 m s^{-1} and (b) 0.5 m s^{-1}. Reproduced from Lee (1999).

culation response to global warming, the available observational evidence suggests that the simulated trends are weaker than observed. For example, observed trends in the SAM index, based on monthly-mean time series, are statistically significant, positive, and about one standard deviation over the last 30 yr (Thompson et al. 2000, Table 10). By contrast, an analysis (details not shown) of the monthly time series of the simulated SAM index in the scenario integrations reveals no significant trends. The trends evident in Figs. 2 and 3 require multiple-year smoothing and emerge significantly only in the twenty-first century. The total SAM-related change in the circulation over the last 100 yr of the integration amounts to roughly half the amplitude of the SAM variability (section 4). Therefore, even though there is a basic agreement of the sign of the trends, their timing and magnitude are not captured by this model. We also recall from section 4 that no significant trends are found in the NAM at any time in the scenario integrations of this model.

The discrepancy between the strength of the simulated and observed trends suggests several urgent research issues. First, the observed SAM trends themselves need to be verified and their significance, in the presence of low-frequency variability, evaluated. Second, the dependence of the coupled model greenhouse-warming response on the details of the stratospheric component of the atmospheric model needs to be resolved. It is plausible that the quality of the stratospheric simulation could impact the wave-mean-flow adjustment and therefore the response throughout the troposphere, as Shindell et al. (1999) have found in their study of the NH response. The simulated upper-level circulation changes are significant under greenhouse warming, even in this model, which only has, roughly speaking, four stratospheric levels. The resulting changes to the transient eddies at upper levels can impact the lower levels through the vertical-mean momentum balance between eddy torques and surface stresses—a form of what is now known as ''downward control'' (Haynes et al. 1991). The wave-mean-flow adjustment and the coupling between the model lower and upper levels might depend sensitively on stratospheric details. Last, the impact of the absence of radiative forcing due to ozone depletion on the scenario integrations needs to be better understood.

Another fundamental research issue that we are pursuing is to understand what determines the direction of the jet shift. One possibility is that the shift is part of a coupled atmosphere–ocean dynamical response that involves changes in lower-tropospheric temperature gradients and the oceanic circulation response depicted in Fig. 13 (Manabe et al. 1991). Another possibility is that the shift is determined, not by changes in the gradients, but by the overall warming or cooling of the ocean surface. This idea is based upon some recent results of Lee (1999). Lee has analyzed a series of integrations of a similar atmospheric GCM to the one used here, but run in a land-free, zonally symmetric, fixed-SST configuration (an ''aquaplanet'' model). Lee finds that a uniform SST increase induces a poleward shift of the jets on the aquaplanet. This shift in the jet is seen in Fig. 14, which is reproduced from Lee (1999). The experiment is run with perpetual annual-mean insolation; the asymmetry between the hemispheres in the figure is associated with sampling error. The expansion of the Hadley cell and gradients in the moisture response might play important roles in the shift.

We have studied a modest, but robust, transient tropospheric response of the Southern Hemisphere circulation to global warming that consists of a poleward shift of the jet and the accompanying general circulation. In the R30 model, the shift is approximately 1° of latitude by the second half of the twenty-first century, and is associated with local wind speed changes of about 5%–10%. Explaining the shift of the jet associated with

global warming and why it is so closely related to the jet's internal variability will require a more basic understanding of the factors controlling the structure of the jet itself. We hope that this line of research will lead not just to an understanding of the atmospheric response to global warming, but, in addition, to a more complete picture of what controls the general circulation of the Southern Hemisphere.

Acknowledgments. We thank J. Fyfe, K. Hamilton, D. Hartmann, S. Lee, and G. Vallis for helpful reviews.

REFERENCES

Bryan, K., S. Manabe, and M. Spelman, 1988: Interhemispheric asymmetry in the transient response of a coupled ocean-atmosphere model to a CO_2 forcing. *J. Phys. Oceanogr.,* **18,** 851–867.

Dai, A., T. Wigley, B. Boville, J. Kiehl, and L. Buja, 2001: Climates of the twentieth and twenty-first centuries simulated by the NCAR Climate System Model. *J. Climate,* **14,** 485–519.

England, M., 1995: Using cholorfluorocarbons to assess ocean climate models. *Geophys. Res. Lett.,* **22,** 3015–3054.

Fyfe, J., G. Boer, and G. Flato, 1999: The Artic and Antarctic Oscillations and their projected changes under global warming. *Geophys. Res. Lett.,* **26,** 1601–1604.

Gent, P. R., and J. C. McWilliams, 1990: Isopycnal mixing in ocean circulation models. *J. Phys. Oceanogr.,* **20,** 150–155.

Hartmann, D. L., and F. Lo, 1998: Wave-driven zonal flow vacillation in the southern hemisphere. *J. Atmos. Sci.,* **55,** 1303–1315.

Haynes, P., C. J. Marks, M. E. McIntyre, T. Shepherd, and K. P. Shine, 1991: On the ''downward control'' of extratropical diabatic circulations by eddy-induced mean zonal forces. *J. Atmos. Sci.,* **48,** 651–678.

Haywood, J., R. Stouffer, R. Wetherald, S. Manabe, and V. Ramaswamy, 1997: Transient response of a coupled model to estimated changes in greenhouse gas and sulfate concentrations. *Geophys. Res. Lett.,* **24,** 1335–1338.

Kattenberg, A., and Coauthors, 1996: Climate models—Projections of future climate. In *Climate Change 1995. The Science of Climate Change,* J. Houghton, L. M. Filho, B. Callander, N. Harris, A. Kattenberg, and K. Maskell, Eds., Cambridge University Press, 285–357.

Knutson, T., T. Delworth, K. Dixon, and R. Stouffer, 1999: Model assessment of regional surface temperature trends (1949–1997). *J. Geophys. Res.,* **104,** 30 981–30 996.

Lee, S., 1997: Maintenance of multiple jets in a baroclinic flow. *J. Atmos. Sci.,* **54,** 1726–1738.

Lee, S.-Y., 1999: Why are the climatological zonal winds easterly in the equatorial upper troposphere? *J. Atmos. Sci.,* **56,** 1353–1363.

Limpasuvan, V., and D. Hartmann, 1999: Eddies and the annular modes of climate variability. *Geophys. Res. Lett.,* **26,** 3133–3136.

Manabe, S., and R. Stouffer, 1996: Low-frequency variability of surface air temperature in a 1000-yr integration of a coupled atmosphere–ocean–land surface model. *J. Climate,* **5,** 284–307.

——, ——, M. Spelman, and K. Bryan, 1991: Transient response of a coupled ocean–atmosphere model to gradual changes of atmospheric CO_2. Part I: Annual mean response. *J. Climate,* **4,** 785–818.

Mitchell, J., T. Johns, J. Gregory, and S. Tett, 1995: Climate response to increasing levels of greenhouse gases and sulphate aerosols. *Nature,* **376,** 501–504.

——, S. Manabe, V. Meleshko, and T. Tokioka, 1990: Equilibrium climate change and its implications for the future. *Climate Change. The IPCC Scientific Assessment.* G. J. J. T. Houghton and J. Ephraums, Eds., Cambridge University Press.

Pacanowski, R. C., K. Dixon, and A. Rosati, 1991: The GFDL Modular Ocean Model users guide version 1. GFDL Ocean Group Tech. Rep. No. 2. NOAA/GFDL. [Available online at ftp://ftp.gfdl.gov/pub/GFDL_MOM.]

Panetta, R. L., 1993: Zonal jets in wide baroclinically unstable regions. *J. Atmos. Sci.,* **50,** 2073–2106.

Rhines, P. B., 1975: Waves and turbulence on a β-plane. *J. Fluid Mech.,* **69,** 417–443.

Shindell, D., R. Miller, G. Schmidt, and L. Pandolfo, 1999: Simulation of recent northern winter climate trends by greenhouse-gas forcing. *Nature,* **25,** 452–455.

——, G. A. Schmidt, R. L. Miller, and D. Rind, 2001: Northern hemisphere winter climate response to greenhouse gas, ozone, solar and volcanic forcing. *J. Geophys. Res.,* in press.

Thompson, D., and J. Wallace, 1998: The Arctic Oscillation signature in the wintertime geopotential height and temperature fields. *Geophys. Res. Lett.,* **25,** 1297–1300.

——, and ——, 2000: Annular modes in the extratropical circulation. Part I: Month-to-month variability. *J. Climate,* **13,** 1000–1016.

——, ——, and G. Hegerle, 2000: Annular modes in the extratropical circulation. Part II: Trends. *J. Climate,* **13,** 1018–1036.

Yu, J.-Y., and D. L. Hartmann, 1993: Zonal flow vacillation and eddy forcing in a simple GCM of the atmosphere. *J. Atmos. Sci.,* **50,** 3244–3259.